

# Plasmonic Enhancement of Dye-Sensitized Solar Cells Using Core–Shell–Shell Nanostructures

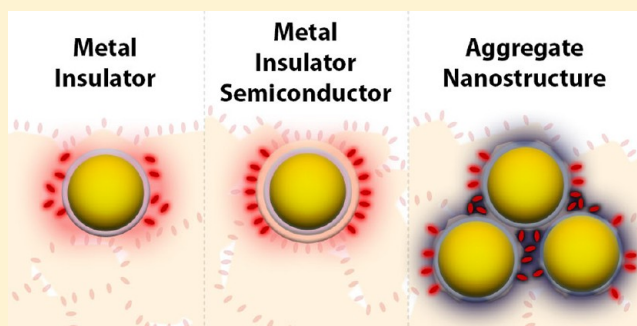
Stafford W. Sheehan,<sup>†</sup> Heeso Noh,<sup>‡</sup> Gary W. Brudvig,<sup>\*,†</sup> Hui Cao,<sup>\*,‡</sup> and Charles A. Schmuttenmaer<sup>\*,†</sup>

<sup>†</sup>Department of Chemistry, Yale University, 225 Prospect St., PO Box 208107, New Haven, Connecticut 06520-8107, United States

<sup>‡</sup>Department of Applied Physics, Yale University, New Haven, Connecticut 06511, United States

## S Supporting Information

**ABSTRACT:** We report the synthesis of core–shell–shell Au@SiO<sub>2</sub>@TiO<sub>2</sub> nanostructures and demonstrate near-field plasmonic enhancement of dye-sensitized solar cells (DSSCs) incorporating them. Isolated nanoparticles as well as nanostructured plasmonic aggregates with broadband light absorption throughout the visible light region are developed. Comparisons to theoretical calculations are performed for the nanoparticles to provide further insight into their structure. We show that Au@SiO<sub>2</sub>@TiO<sub>2</sub> nanoparticles provide efficiency enhancements greater than that of Au@SiO<sub>2</sub> plasmonic nanoparticles and vary the distance between the molecular chromophore and the gold NP surface to demonstrate that this arises from near-field plasmonic effects. Finally, enhancement of dye absorption in DSSCs using a coupled plasmonic system is shown for the first time and results in a broadband enhancement of quantum efficiency.



## INTRODUCTION

Nanostructures made of noble metals have long been used to manipulate light on a subwavelength scale. This has led to numerous applications in spectroscopy,<sup>1</sup> optics,<sup>2</sup> and many other fields.<sup>3,4</sup> Solar cells in particular are dependent on efficient harnessing of light for conversion to electricity or chemical fuel, and this has recently opened the field of plasmonic enhancement applied to solar cells.<sup>5,6</sup> Of the types of solar cells being researched, dye-sensitized solar cells (DSSCs) are a promising alternative to traditional solar cells and are particularly amenable to incorporation of plasmonic nanoparticles. Similar concepts can also be extended toward plasmonic enhancement of other types of solar cells, such as organic,<sup>7</sup> silicon,<sup>5</sup> and water-splitting systems.<sup>8</sup> In order to best integrate them into a TiO<sub>2</sub> nanoparticle-based DSSC, we created a nanostructure comprised of a plasmonic Au nanoparticle encapsulated in a SiO<sub>2</sub> shell followed by a TiO<sub>2</sub> shell. The SiO<sub>2</sub> shell electronically insulates the Au core and also protects it from corrosion or other deleterious effects. The TiO<sub>2</sub> layer allows these NPs to be seamlessly incorporated into nanoscale mesoporous TiO<sub>2</sub>-based photoanodes used in dye-sensitized photocatalytic or photoelectrochemical solar cells. It is essential that the SiO<sub>2</sub> and TiO<sub>2</sub> shells are thin enough that chromophores bound to the Au@SiO<sub>2</sub>@TiO<sub>2</sub> nanoparticles experience near-field plasmonic enhancement.

Recent studies have shown that plasmonic enhancement is indeed a viable path toward improving DSSCs. Using plasmonics to concentrate light, it is possible to reduce the thickness of the mesoporous TiO<sub>2</sub> working electrode without hindering absorption.<sup>9</sup> This reduces the distance charges must

travel to reach the external circuit and lessens the probability of charge recombination. The first technological hurdle to overcome in this design is that bare metallic nanoparticles are shown to both corrode and facilitate carrier recombination in DSSCs,<sup>10</sup> requiring them to be insulated from the surrounding electrolyte.<sup>11</sup> Subsequent work incorporating an insulating SiO<sub>2</sub> shell around a metal nanoparticle provided a partial solution to this problem,<sup>12</sup> however, molecular dyes cannot inject charges into SiO<sub>2</sub>, which reduces the potential effectiveness of the plasmonic nanoparticle. This issue of charge injection can be resolved by coating nanoparticles instead with TiO<sub>2</sub> before incorporating them into a DSSC, a strategy which has met with some success.<sup>9</sup> However, chemical insulation of metal nanoparticles that does not also provide electrical insulation opens up the metal core to charging effects, which have been shown to increase the efficiency less than plasmonic effects.<sup>13</sup> Plasmonic enhancement of DSSCs has also been demonstrated with both smaller<sup>14</sup> and larger Au nanoparticles,<sup>15</sup> Au@TiO<sub>2</sub> hollow submicrospheres,<sup>16</sup> and Au@Ag<sub>2</sub>S nanorods,<sup>17</sup> though many issues remain unresolved.

In our demonstration, we utilize a new structure combining the advantage of an insulating SiO<sub>2</sub> coating with a photoconductive TiO<sub>2</sub> shell. The resulting multilayered nanoparticle provides a greater enhancement to DSSC performance compared to using single shells. We demonstrate this by building devices with thin working electrodes to show that our new approach overcomes the problems outlined previously. We

Received: December 10, 2012

Published: December 17, 2012

find the greatest improvements to device performance when nanostructures made by controlled aggregation of Au@SiO<sub>2</sub> nanoparticles were added to a DSSC. We attribute this to both the broadband absorption of these structures<sup>18–20</sup> and the larger dipole moments brought about by coupled surface plasmon resonance modes.<sup>19,21</sup>

Gold was chosen as a metallic core for our system because the localized surface plasmon resonance (LSPR) in Au nanoparticles (NPs) occurs in the vicinity of 525 nm. Furthermore, the peak wavelength of the LSPR increases as the refractive index of the surrounding medium increases.<sup>22–24</sup> Thus, it is possible to achieve a maximum in the nanoparticle's extinction spectrum near the maximum absorbance of the most commonly used dye for DSSCs, N719, at 530 nm. While the peak position of the LSPR is barely dependent on the Au NP radius in the range 5–20 nm, the near-field plasmonic enhancement increases significantly with decreasing particle size.<sup>4</sup>

On the basis of the considerations given above, we have synthesized spherical Au NPs with a 9 nm radius and added a SiO<sub>2</sub> shell roughly 1.6 nm thick. We compare the performance when growing TiO<sub>2</sub> shells that are ~2.5 and ~7.0 nm thick. The optical properties of solutions of these NPs depend on the nature of the shell(s) and surrounding medium and are successfully simulated.

We constructed DSSCs consisting of sintered P25 TiO<sub>2</sub> NPs sensitized with N719 using an I<sub>3</sub><sup>−</sup>/I<sup>−</sup> redox shuttle and compared their performance in the absence and presence of Au@SiO<sub>2</sub>, Au@SiO<sub>2</sub>@TiO<sub>2</sub> with both thin and thick TiO<sub>2</sub> layers, and Au@SiO<sub>2</sub>@TiO<sub>2</sub> aggregates. The DSSC efficiency increases when incorporating each type of these plasmonic NPs and does so most dramatically for the ones with a thin TiO<sub>2</sub> shell and the aggregates.

One general advantage of incorporating nanoparticles into DSSCs is that they provide far-field scattering and concomitant enhancement due to longer effective optical path lengths.<sup>5</sup> There have been previous reports of incorporating metal core@shell NPs into DSSCs, where the metal core is Au or Ag and the shell is SiO<sub>2</sub> or TiO<sub>2</sub>.<sup>9,12–14,25</sup> There have also been theoretical studies of multilayered structures,<sup>26</sup> but no experimental data as of yet. Encapsulating metal NPs in a shell serves three purposes: (1) If the shell is an insulator, it can electrically insulate the Au NP from its surroundings. This is important because bare Au NPs trap electrons and facilitate reduction of I<sub>3</sub><sup>−</sup> to I<sup>−</sup> thereby acting as a loss mechanism.<sup>12</sup> (2) It is possible to grow very thin shells that allow the dye molecules to be in close enough proximity to the metal NP for plasmonic enhancement. (3) The shell provides a physical barrier to the I<sub>3</sub><sup>−</sup> which is corrosive toward Au.<sup>27,28</sup>

Rather than utilizing a single shell, we chose the core@shell@shell architecture to benefit from both types of shells. Specifically, if the TiO<sub>2</sub> layer is not used, then the dye molecules most influenced by the plasmonic enhancement are physisorbed rather than chemisorbed on the SiO<sub>2</sub> shell, and its band gap is too large to allow electron injection. We note, however, that improvements have been reported for this structure nonetheless.<sup>12,13</sup> This is due to dye molecules bonded to TiO<sub>2</sub> NPs in the mesoporous network that happen to be in close proximity to the Au@SiO<sub>2</sub> NPs. However, when a TiO<sub>2</sub> shell is grown on top of the SiO<sub>2</sub> shell as is reported here, electrons can be injected directly into the TiO<sub>2</sub> shell that incorporates the NPs into the photoanode. Very thin shells are required since the near-field plasmonic enhancement decreases

rapidly as a function of distance from the Au surface,<sup>29,30</sup> and it is shown here that the thin TiO<sub>2</sub> shell outperforms the thick one.

Finally, we find that Au@SiO<sub>2</sub>@TiO<sub>2</sub> aggregates provide the highest increase in DSSC efficiency. This is attributed to two factors: (1) The localized surface plasmons in individual particles are coupled to form surface plasmon resonances over a broad frequency range, thus enhancing light absorption over a wider frequency range than isolated NPs.<sup>31</sup> (2) Most of the coupled surface plasmon resonances have larger dipole moments than those of a single NP, producing a higher local field.<sup>32–36</sup>

## ■ EXPERIMENTAL METHODS

Au nanoparticles with a thin SiO<sub>2</sub> shell were synthesized following previously published methods.<sup>12,22</sup> To synthesize the Au core, the Turkevich method was employed.<sup>37</sup> A solution of 0.02% w/w hydrogen tetrachloroaurate (III) trihydrate in deionized water (150 mL) was heated to boil, to which 6.5 mL of a solution of 1% w/w citric acid (trisodium salt dihydrate) was added while stirring. The solution rapidly turned black and after ~75 s became a dark red-orange color which indicated the formation of Au nanoparticles. The solution was boiled for an additional 15 min to ensure that the reaction proceeded to completion and was then removed from the heat and allowed to cool to room temperature.

To grow conformal SiO<sub>2</sub> shells, the citrate adsorbate surrounding the Au nanoparticles was exchanged with 3-aminopropyltriethoxysilane (APTES) by adding 1.5 mL of a 1.92 μM APTES solution dropwise over 30 min while vigorously stirring. The solution sat without stirring for an additional 30 min before addition of 5.5 mL of 0.54% w/w sodium silicate with pH reduced to 10.26 using a Dowex HCR-S cation-exchange resin. This solution then sat for 36 h, allowing the SiO<sub>2</sub> shells to grow before being centrifuged at 3150 rpm (Fischer, 614b) and redispersed via sonication into 200 proof ethanol, thereby ending shell growth.

Synthesis of TiO<sub>2</sub> shells on these Au@SiO<sub>2</sub> nanoparticles followed methods previously described for TiO<sub>2</sub> shell growth with small modifications.<sup>9,38</sup> For thinner shells (roughly 2.5 nm), 1 mL of 4% ammonia in ethanol was added to 10 mL of Au@SiO<sub>2</sub> nanoparticles at 1.5 times their original concentration. 5 μL of Ti[OHC(CH<sub>3</sub>)<sub>2</sub>]<sub>4</sub>, denoted Ti(O<sup>i</sup>Pr)<sub>4</sub>, in 3 mL of ethanol was then added to the solution, which was stirred for 12 h and then sonicated for 30 min. 15 μL of Ti(O<sup>i</sup>Pr)<sub>4</sub> was hydrolyzed in 1 mL of 95% ethanol and added to the nanoparticle solution while sonicating to ensure that the same amount of Ti(O<sup>i</sup>Pr)<sub>4</sub> was added to both thin and thick shell solutions. For thicker shells (roughly 7.0 nm), 1 mL of 4% ammonia in ethanol was added to 10 mL of Au@SiO<sub>2</sub> nanoparticles at 1.5 times their original concentration, after which 5 μL of Ti(O<sup>i</sup>Pr)<sub>4</sub> in 1 mL of ethanol was slowly added to begin a thin shell growth. 10 mg of hydroxypropyl cellulose was slowly added to the solution, which was stirred for 1 h and then sonicated for 15 min. Another 5 μL of Ti(O<sup>i</sup>Pr)<sub>4</sub> in 1 mL of ethanol was added to the solution, and it was stirred for 30 min, followed by sonication for 5 min. This process was repeated two more times such that a total of 20 μL of Ti(O<sup>i</sup>Pr)<sub>4</sub> was added to the solution, and the nanoparticle solution was then stirred for 12 h. The samples with 2.5 and 7.0 nm TiO<sub>2</sub> layers are referred to as “Au@SiO<sub>2</sub>@TiO<sub>2</sub> (thin)” and “Au@SiO<sub>2</sub>@TiO<sub>2</sub> (thick)”, respectively.



In order to form random nanoparticle aggregates, the concentration of Au@SiO<sub>2</sub> nanoparticles in ethanol was doubled via centrifugation and then sonicated for 15 min. 20 mL of the concentrated nanoparticle solution was vigorously stirred while 1 mL of ethanol containing 10  $\mu$ L of Ti(O<sup>i</sup>Pr)<sub>4</sub> was rapidly added to it. The solution changed color from red to bluish-purple. Within the next 2 h, the solution continued darkening until it turned pitch black, signifying formation of the nanostructures. Vigorous stirring or sonication is required in order to aerate the solution and introduce a small amount of water into the dry ethanol, allowing the titanium precursor to hydrolyze sufficiently to form aggregates. While a TiO<sub>2</sub> layer was not intentionally grown on them, a very thin and nonuniform layer forms when the Ti(O<sup>i</sup>Pr)<sub>4</sub> is added to induce aggregation (Figure S1).

Synthesis of Pt counter electrodes and I<sub>3</sub><sup>-</sup>/I<sup>-</sup> electrolyte solution for solar cells followed a previously published procedure.<sup>39</sup> In order to make a plasmonic TiO<sub>2</sub> paste used in doctor-blading onto fluorine-doped tin oxide (FTO) for DSSC photoanodes and glass microscope slide coverslips for UV-vis measurements, 0.1 mL of 1% acetic acid in water was added to 2 mL of nanoparticle solution and sonicated for 10 min. P25 TiO<sub>2</sub> nanoparticles (Evonik/Degussa) were slowly added during sonication to ensure paste homogeneity. 500 mg of P25 per 2 mL of ethanol solution was added to pastes without nanoparticles and with Au@SiO<sub>2</sub> nanoparticles, while 250 mg of P25 was used per 2 mL of TiO<sub>2</sub>-shelled nanoparticle solutions. Pastes were then carefully doctor-bladed onto coverslips and FTO using a 0.25 cm<sup>2</sup> template for the working electrode active area. This yielded films approximately 10–12  $\mu$ m thick. After coating, samples were heated to 400 °C for 2 h to allow particle sintering without the formation of rutile in the TiO<sub>2</sub> shells. After sintering, the nanoparticles were immersed in a 0.2 mM ethanol solution of N719 dye [ditetrabutylammonium *cis*-bis(isothiocyanato)bis(2,2'-bipyridyl-4,4'-dicarboxylato)ruthenium(II)] for 24 h.

Characterization of the nanoparticles was carried out using scanning electron microscopy (SEM), transmission electron microscopy (TEM), and UV-vis spectrophotometry. Low-resolution TEM images were taken using a Zeiss EM-900 operating at 80 kV while high-resolution TEM images and scanning TEM/energy dispersive X-ray (STEM/EDX) mapping was performed using an FEI Tecnai Osiris operating at 200 kV. A Hitachi SU-70 was used to take SEM images. UV-vis measurements were taken using a Varian Cary 3 spectrophotometer. Spectra of dyed samples on microscope slide coverslips were determined with an integrating sphere in diffuse reflectance mode by measuring transmittance and reflectance separately and then calculating the absorbance using  $A = 1 - R - T$ .

DSSCs were assembled using a 60  $\mu$ m plastic thermal spacer (SX1170-60, Solaronix SA, Switzerland) to contain the electrolyte by sandwiching it between the electrodes and held together with metal binder clips. Photocurrent–voltage scans were taken using a Keithley 2400 source meter, and a 300 W ozone-free xenon lamp equipped with an AM 1.5G filter (Newport) was used as the light source. The light intensity was adjusted to 1-sun conditions (100 mW/cm<sup>2</sup>) prior to scanning. Incident photon-to-current efficiency (IPCE) measurements were made with a PV Measurements Inc. Solar Cell Spectral Response Measurement System (Model QEXY), calibrated between 300 and 1000 nm using a silicon photodiode. A chopping speed of 5 Hz was used during both calibration and

measurement. Exact TiO<sub>2</sub> photoanode areas were determined using a 1200 dpi scanner.

## RESULTS AND DISCUSSION

The SiO<sub>2</sub> shell was grown as thin as possible without the formation of holes or significant loss of surface coverage as determined by TEM imaging. The near-field nature of LSPR and the fact that the TiO<sub>2</sub> outer shell must be thick enough to allow facile charge transfer and transport render a thin SiO<sub>2</sub> shell critically important. The slow growth afforded by lowering the pH of the sodium silicate precursor and controlling its concentration ensures that the shell is as conformal as possible. Figures 1a and 1b show Au nanoparticles before and after

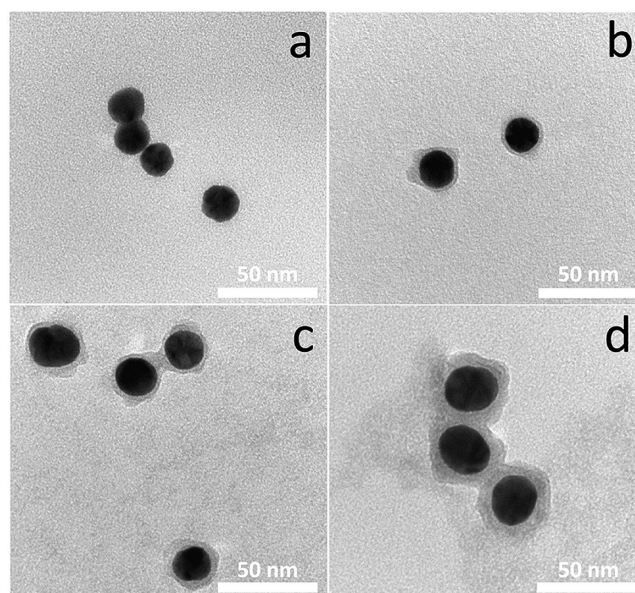


**Figure 1.** Citrate-stabilized gold nanoparticles (a), along with nanoparticles from the same batch after coating with silica (b), then further with a thin titania coating ( $\sim 2.5$  nm) (c), and thick titania coating ( $\sim 7.0$  nm) (d). Scale bars are all 50 nm.

growth of the SiO<sub>2</sub> shell, respectively. The thickness of the shell is  $\sim 1.6$  nm. While some tunneling may occur, we found when incorporating them in to solar cells that the majority of electronic communication between TiO<sub>2</sub> and Au was inhibited.

Growth of the TiO<sub>2</sub> shell also required pH control of the solution by a low concentration of ammonia in ethanol. If concentrations were too low, nanoparticles were prone to aggregate together rather than simply grow TiO<sub>2</sub> shells. As shown in Figures 1c and 2a, the thin TiO<sub>2</sub> shells are typically quite jagged which may provide more surface area for dye coverage but can also impede electron transport. Thicker TiO<sub>2</sub> shells were also grown (Figure 1d) and have smoother surfaces in addition to their increase in overall thickness. Dimensions of the Au NPs and metal oxide shell(s) were obtained by image analysis of 100 NPs of each type and are given in Table S1.

TEM, EDX, and STEM/EDX mapping were used to confirm the morphology of the Au@SiO<sub>2</sub>@TiO<sub>2</sub> nanostructures. Figure 2a is a HRTEM image of a dual-shelled nanoparticle with a smooth SiO<sub>2</sub> layer, covered by a jagged TiO<sub>2</sub> layer, and Figure 2b shows an EDX map of nanoparticles which clearly reveal a gold core (green) surrounded by a SiO<sub>2</sub> shell (blue), which is then encapsulated by TiO<sub>2</sub> (red). Additional EDX spectra,

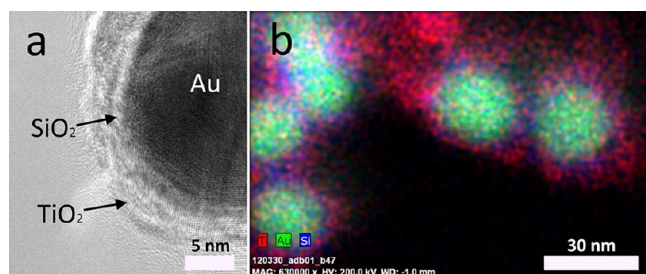


**Figure 2.** (a) HRTEM image of an Au@SiO<sub>2</sub>@TiO<sub>2</sub> (thin) NP showing both inner SiO<sub>2</sub> and outer TiO<sub>2</sub> shells; scale bar: 5 nm. (b) STEM-EDX map of Au@SiO<sub>2</sub>@TiO<sub>2</sub> (thin) NPs showing an Au core (Au shown in green), a conformal SiO<sub>2</sub> inner shell (Si shown in blue), and a jagged TiO<sub>2</sub> outer shell (Ti shown in red); scale bar: 30 nm.

TEM images, and characterization of the NPs and aggregates are included in the Supporting Information.

Experimental and calculated UV–vis extinction spectra for Au and Au@SiO<sub>2</sub> NPs in water and Au@SiO<sub>2</sub>@TiO<sub>2</sub> (thin) NPs and aggregates in ethanol are shown in Figure 3. Mie

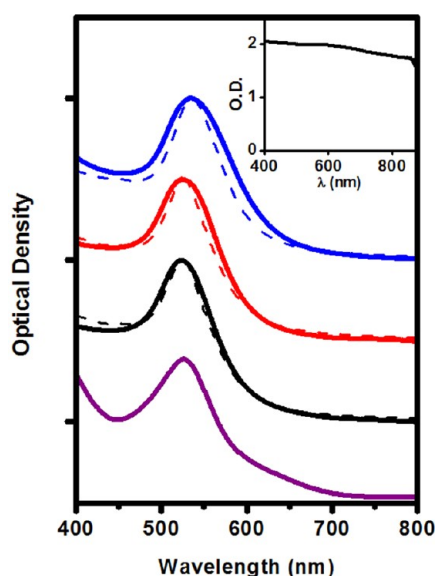


**Figure 3.** Experimental (solid lines) and calculated (dashed lines) UV–vis spectra of nanoparticles in solution showing a red shift in plasmon resonance peak position as shells are added. APTES-stabilized Au NPs, Au@SiO<sub>2</sub> NPs, and Au@SiO<sub>2</sub>@TiO<sub>2</sub> (thin) NPs are represented by black, red, and blue traces, respectively. The purple curve at the bottom shows the absorption spectrum of N719 for comparison. Inset: absorption spectrum of nanostructured aggregates formed from Au@SiO<sub>2</sub> NPs, showing broadband absorption of visible light.

theory is used to calculate the spectra<sup>40</sup> using the wavelength-dependent complex refractive index of bulk Au<sup>41</sup> and are in excellent agreement with the measured spectra. Refractive indices for SiO<sub>2</sub> and TiO<sub>2</sub> of 1.461 and 2.488 were used, respectively, and assumed to be constant over the frequency range of interest. Similarly, the refractive indices of water and ethanol were held fixed at 1.333 and 1.361, respectively.

The calculated peak width is too narrow when only free electron scattering in the bulk metal is assumed. However, as the NP size approaches the mean free path of free electrons in Au, the scattering rate increases<sup>42</sup> and the value of the dielectric

constant changes. Specifically, the frequency-dependent dielectric function,  $\epsilon$ , is given by<sup>43</sup>

$$\epsilon(\omega) = \epsilon_B(\omega) + \epsilon_D(\omega) \quad (1)$$

The frequency is denoted  $\omega$ ,  $\epsilon_B(\omega)$  is due to bound electrons, and  $\epsilon_D(\omega)$  is due to free electrons which are assumed to obey Drude behavior. Furthermore, the Drude term is expressed as<sup>43</sup>

$$\epsilon_D(\omega) = 1 - \frac{\omega_p^2}{\omega^2 + i\gamma\omega} \quad (2)$$

where  $\gamma$  is the damping coefficient and  $\omega_p$  is the plasmon frequency  $\omega_p = ne^2/\epsilon_0 m_{\text{eff}}$  ( $n$  is the electron density,  $e$  is the magnitude of the electron charge,  $\epsilon_0$  is the permittivity of free space, and  $m_{\text{eff}}$  is the electron effective mass). In the bulk, the damping coefficient  $\gamma$  is given by  $\gamma_0 = v_F/l_\infty$ , where  $v_F$  is the Fermi velocity and  $l_\infty$  is the bulk mean free path.<sup>44</sup> In a NP, the damping coefficient depends on particle size, and for a spherical particle with isotropic scattering it becomes<sup>43</sup>

$$\gamma_R = \gamma_0 + \frac{A v_F}{R} \quad (3)$$

where  $A$  is a dimensionless parameter typically near unity and  $R$  is the NP radius. Thus, the bulk complex permittivity values,  $\epsilon_{\text{bulk}}$ , from ref 41 (obtained from  $\epsilon' = n^2 - k^2$  and  $\epsilon'' = -2nk$ , since  $n^2 = \epsilon$ ) are corrected for the additional scattering term using

$$\epsilon_{\text{NP}}(\omega, R) = \epsilon_{\text{bulk}} - \left( 1 - \frac{\omega_p^2}{\omega^2 + i\gamma_0\omega} \right) + \left( 1 - \frac{\omega_p^2}{\omega^2 + i\gamma_R\omega} \right) \quad (4)$$

The value of  $A$  is fixed at  $(\pi/2)^{1/3}$ , or 1.16, for the calculated spectra in Figure 3.<sup>42</sup> The SiO<sub>2</sub> and TiO<sub>2</sub> shells red-shift the localized surface plasmon resonance; the TiO<sub>2</sub> shell shifts it by a greater amount than SiO<sub>2</sub> because the difference between its refractive index and that of the surrounding medium is greater than for SiO<sub>2</sub>. The average SiO<sub>2</sub> shell thickness is determined to be 1.6 nm from TEM images. There is a bit of porosity, however, so its effective refractive index,  $n_{\text{eff}}$ , is smaller than the bulk value and is given by<sup>45</sup>

$$n_{\text{eff}} = \sqrt{f\epsilon_{\text{MO}_2} + (1-f)\epsilon_m} \quad (5)$$

where  $\epsilon_{\text{MO}_2}$  is the permittivity of the metal oxide,  $f$  is its volume fraction, and  $\epsilon_m$  is fixed at 1.0. A 92% volume fraction of SiO<sub>2</sub> in the shell results in excellent agreement between the calculated and measured peak position of Au@SiO<sub>2</sub> NPs in water. Similarly, we compared the calculated extinction spectrum of Au@SiO<sub>2</sub>@TiO<sub>2</sub> NPs in ethanol to the measured one. In this case, the peak center moves to 634 nm, and the volume fraction of TiO<sub>2</sub> in the 2.5 nm shell is 65%. The relatively low volume fraction is partly due to the nonuniform thickness of the TiO<sub>2</sub> shell.

The aggregate nanostructures have broadband absorption throughout the visible spectral region due to coupled plasmon modes, which results in their deep black color (a photograph is shown in Figure S7). The absorption is broadband due to a large distribution in interparticle distances among the randomly aggregated particles,<sup>19</sup> in addition to small variations in SiO<sub>2</sub> shell thickness and excess TiO<sub>2</sub> used to form them.



The DSSCs constructed were found to have a uniform dispersion of NPs throughout their working electrodes. Figure 4 is an edge-on SEM micrograph of a 12  $\mu\text{m}$  thick doctor-

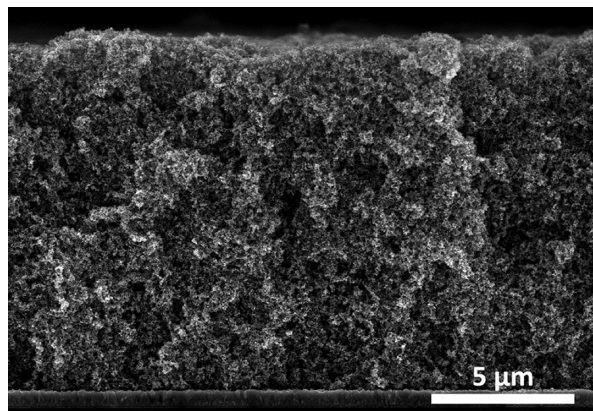


**Figure 4.** SEM image of a P25  $\text{TiO}_2$  film on FTO/glass with  $\text{Au@SiO}_2$  NPs embedded. Scale bar: 5  $\mu\text{m}$ .

bladed film with  $\text{Au@SiO}_2$  NPs incorporated;  $\text{Au@SiO}_2$  NPs tend to appear with a higher contrast than P25  $\text{TiO}_2$ . Relative concentrations of NPs are represented in Figure S4, which shows the absorbance spectra ( $1 - R - T$ ) of doctor-bladed films before being immersed in dye. The films are  $\sim 0.1\%$  w/w Au, which is a typical concentration for which plasmonic enhancement is seen in DSSCs.<sup>12</sup> Figure 5a compares IPCE results for DSSCs incorporating  $\text{Au@SiO}_2$ ,  $\text{Au@SiO}_2@\text{TiO}_2$  (thin),  $\text{Au@SiO}_2@\text{TiO}_2$  aggregates, and one that does not contain any NPs. It is seen that all of the samples with NPs perform better than those without. The  $\text{Au@SiO}_2@\text{TiO}_2$  samples perform better than the  $\text{Au@SiO}_2$  ones, and the aggregates provide the highest IPCE of all. The peak of the IPCE curve does not shift significantly for the different samples, which is consistent with their UV-vis absorbance spectra. It is important to note that the LSPR modes of the nanoparticles have been matched to the N719 peak absorption wavelength through their size control and choice of gold over silver. In addition, the aggregates couple with the dye at wavelengths longer than the peak value of 530 nm, which is due to the dye interacting with the coupled LSPR modes of multiple metal nanoparticles in the aggregates.

Figure 5b displays their absorbance spectra after being immersed in N719 dye, and it is seen that they follow the same general trend as the IPCE curves except for the aggregates at wavelengths longer than 700 nm. At these wavelengths, the aggregates themselves absorb light but the dye sensitizer does not, so electrons will not be injected into the semiconductor and thus will not contribute to the IPCE. Careful inspection reveals that this also occurs to a lesser extent with the  $\text{Au@SiO}_2$  and  $\text{Au@SiO}_2@\text{TiO}_2$  (thin) samples. It is seen that NPs enhance the maximum IPCE by a factor of 1.2–1.6 and the maximum absorbance by a factor of 1.2–1.5.

Current–voltage ( $J$ – $V$ ) curves were measured for DSSCs that were constructed without any metal NPs, those incorporating  $\text{Au@SiO}_2$ , with  $\text{Au@SiO}_2@\text{TiO}_2$  (thin),  $\text{Au@SiO}_2@\text{TiO}_2$  (thick), and aggregates. Nine samples of each type were made. The best one of each type is shown in Figure 6a, and the averages are shown in Figure 6b. The usual solar cell parameters of open-circuit voltage,  $V_{\text{oc}}$ , short-circuit current,  $J_{\text{sc}}$ , fill factor, and efficiency are reported in Table 1, while standard deviations are reported in Table S2 and are plotted together in Figure S8.

P25  $\text{TiO}_2$  dispersed in ethanol without any metal nanoparticles and doctor-bladed onto the substrate resulted in highly porous films  $\sim 12 \mu\text{m}$  thick. After being immersed in the N719 dye solution, the films remained moderately transparent, as shown in Figure 5b. This partially accounts for their low DSSC efficiency compared to films made using additional preparation procedures such as  $\text{TiCl}_4$  treatments, thicker active layers, optimization of  $\text{TiO}_2$  paste, and light-scattering layers,<sup>46</sup> which we omitted in this initial proof of concept.

Addition of  $\text{Au@SiO}_2$  nanoparticles to the  $\text{TiO}_2$  paste during fabrication increases  $J_{\text{sc}}$  and the efficiency due to plasmonic enhancement, as has been seen in previous studies.<sup>12,13</sup> The DSSCs made from  $\text{Au@SiO}_2@\text{TiO}_2$  (thin) and the aggregates have the best efficiencies and  $J_{\text{sc}}$  values.

The DSSC incorporating the aggregates is the first demonstration of enhancement of efficiency using plasmonic nanoparticles coupled with each other (in addition to the surrounding dye). In this case, the enhancement in overall efficiency is a result of an increase in both  $V_{\text{oc}}$  and  $J_{\text{sc}}$ . This may be a contribution from the high electromagnetic fields caused by the coupled plasmonic modes in the aggregates because the coupled surface plasmon modes typically have larger dipole moments than the uncoupled ones in isolated NPs.<sup>21,33</sup> Overall, the aggregates improve the efficiency of these DSSCs from

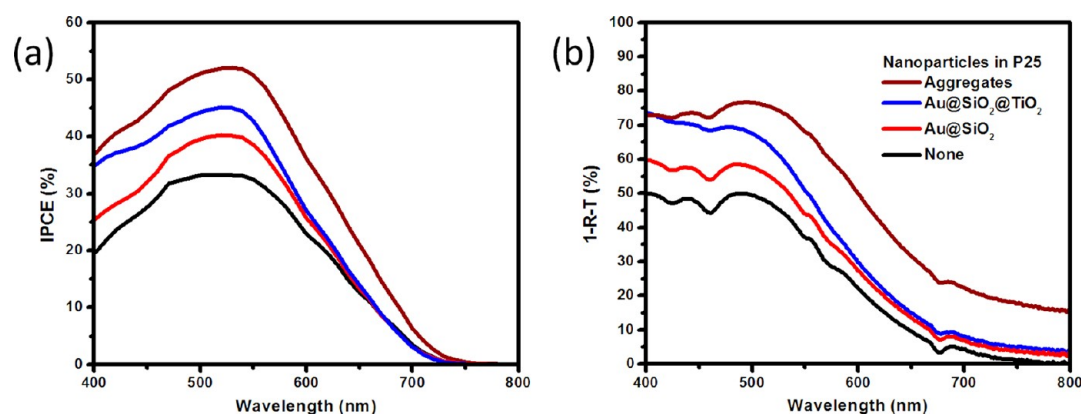


**Figure 5.** IPCE (a) and absorbance spectra (b) with different plasmonic NPs embedded in  $\text{TiO}_2$  electrodes containing  $\sim 0.1\%$  w/w Au. Measurements were made on samples with efficiencies most similar to their “average” in Table 1.

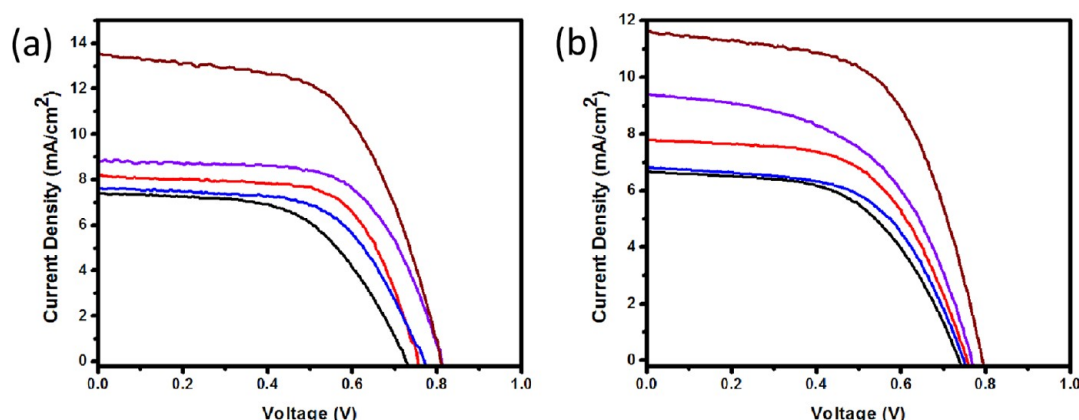


**Figure 6.**  $J$ – $V$  curves for solar cells made with no NPs in P25  $\text{TiO}_2$  (black),  $\text{Au@SiO}_2$  (red),  $\text{Au@SiO}_2\text{@TiO}_2$  thin (purple),  $\text{Au@SiO}_2\text{@TiO}_2$  thick (blue), and aggregates (maroon). (a) shows the best solar cells incorporating each type of nanoparticle, while (b) depicts an average of the nine curves in each batch.

**Table 1.** Averages for Each Parameter Contributing to Solar Cell Efficiency in Addition to Best Efficiency Values; Total Shell Thicknesses for the Nanoparticles Are Included in Parentheses

nanoparticles in P25	$V_{oc}$ (V)	$J_{sc}$ ( $\text{mA}/\text{cm}^2$ )	FF (%)	av efficiency (%)	best efficiency (%)
none	0.746	6.64	56.8	2.81	3.07
$\text{Au@SiO}_2$ (1.6 nm)	0.753	7.78	60.3	3.52	4.04
$\text{Au@SiO}_2\text{@TiO}_2$ (4.1 nm)	0.773	9.37	57.0	4.02	4.60
$\text{Au@SiO}_2\text{@TiO}_2$ (8.6 nm)	0.754	6.81	58.2	2.99	3.54
aggregates	0.804	11.59	59.3	5.52	6.42

2.81% (no metal NPs) to 5.52%. This is the largest reported improvement of DSSC absolute efficiency due to plasmonic enhancement to our knowledge and the first demonstration of using a coupled plasmonic system to improve a DSSC.

The DSSCs with  $\text{Au@SiO}_2\text{@TiO}_2$  (thick) NPs perform very similarly to the standard DSSC without any NPs at all (Figure 6b). They are identical to those containing  $\text{Au@SiO}_2\text{@TiO}_2$  (thin) NPs except that the  $\text{SiO}_2$  and  $\text{TiO}_2$  combined shell thickness is 8.6 nm compared to 4.1 nm for the thin-shelled NPs. This demonstrates that the enhancement when using  $\text{Au@SiO}_2\text{@TiO}_2$  (thin) is a near-field plasmonic effect since it is extremely sensitive to distance from the Au metal core. The DSSCs with  $\text{Au@SiO}_2\text{@TiO}_2$  (thick) NPs have a slightly higher efficiency than those without any NPs at all, which indicates a small amount of far-field plasmonic enhancement due to scattering. Roughness of the outer  $\text{TiO}_2$  shell also plays a role in performance of the samples containing thick vs thin  $\text{TiO}_2$  shells. The thin  $\text{TiO}_2$  shells have higher roughness than the thick ones, which results in a larger surface area for dye adsorption. More importantly, the molecules found at the bottom of the shallow regions experience much stronger plasmonic near-field enhancement.

It is useful to model the DSSC behavior to better understand the underlying changes that affect the measured cell parameters ( $V_{oc}$ ,  $J_{sc}$ , fill factor, and efficiency). The standard description of a diode solar cell has been applied successfully to DSSCs by many authors and is given by<sup>47</sup>

$$J = J_L - J_D - J_{SH}$$

$$J = J_L - J_0 \left\{ \exp \left[ \frac{q(V + JAR_S)}{fk_B T} \right] - 1 \right\} - \frac{V + JAR_S}{AR_{SH}} \quad (6)$$

where  $J$  is the net current density,  $J_L$  is the photocurrent density,  $J_0$  is the reverse saturation current density,  $V$  is the applied voltage,  $R_S$  and  $R_{SH}$  are the series resistance and shunt resistance of the cell, respectively,  $A$  is the area of the cell,  $q$  is the magnitude of the electron charge,  $k_B$  is Boltzmann's constant,  $f$  is the ideality factor (which is fixed at 2), and  $T$  is the temperature, which is fixed at 298 K. The series resistance arises from resistances of the photoanode, transparent conducting electrodes, and electrolyte solution. Higher values of  $R_S$  decrease the cell efficiency primarily by decreasing the fill factor but also to a lesser extent through a reduction in  $J_{sc}$ . Smaller values of  $R_{SH}$  allow the parasitic shunt current,  $J_{SH}$ , to increase which degrades the overall performance, primarily through a decrease in the fill factor. The shunt current arises from losses due to carrier recombination with the oxidized dye molecule and/or direct recombination with the redox couple.

This model was fit to the experimental  $J$ – $V$  curves for the best devices and for the average performance. The agreement between the model and the experimental data is quite good as seen in Figure S9, and the parameters obtained are given in Table S3. The overall trends in DSSC performance are dominated by the behavior of  $J_L$ , but  $J_0$  also plays a minor role.  $R_S$  and  $R_{SH}$  have much smaller influence. If there is a decrease in the reverse saturation current,  $J_0$ , which is due electrons traveling “backwards” from the conduction band to the excited state energy level of the dye molecules, then  $V_{oc}$  will increase with no change in  $J_{sc}$ . An increase in  $J_L$ , which is caused by higher electron injection rates, will simply shift the entire  $J$ – $V$  curve upward (as long as  $R_S$  is small and  $R_{SH}$  is large, as is the case here), causing both  $J_{sc}$  and  $V_{oc}$  to increase. There is an additional limit regarding how much  $V_{oc}$  may increase since it can be no larger than the difference between the  $\text{TiO}_2$  Fermi level and the  $\text{I}_3^-/\text{I}^-$  reduction potential. Since the aggregates have significantly higher values of  $J_L$  due to interparticle plasmonic coupling, they significantly outperform the other samples.

## CONCLUSION

In summary, we have synthesized a new type of nanostructure using a metal–insulator–semiconductor design to insulate and protect plasmonic nanoparticles while simultaneously incorporating a photoactive semiconductor as its outermost layer. In addition, we constructed a metal–insulator aggregate system, which allows nanoparticles to couple with each other forming LSPR modes that show broadband absorption throughout the visible light region.

We have shown that the metal–insulator–semiconductor nanoarchitecture can be successfully incorporated into DSSCs to yield improvements beyond those of a metal–insulator system due to the closer proximity of dye molecules to the metal surface. We have demonstrated quenching of the plasmonic enhancement by increasing the semiconductor shell thickness, thereby establishing that the enhancement arises from near-field effects, namely LSPR modes. Broadband enhancement of dye absorption in DSSCs is shown using a coupled plasmonic system resulting in an increase in efficiency from 2.81% to 5.52% on average when compared to those made without metal nanoparticles. After this initial proof of concept, our future studies will include optimizing and incorporating these black plasmonic aggregates into higher efficiency DSSCs.

The Au@SiO<sub>2</sub>@TiO<sub>2</sub> architecture is amenable to other types of solar cells by using a different semiconductor for the active layer or by inducing aggregation with materials other than TiO<sub>2</sub>. In addition, the broadband plasmonic enhancement afforded by the aggregates can be used in other spectroscopic applications, such as fluorescence, Raman scattering, and second harmonic generation.<sup>48</sup>

## ASSOCIATED CONTENT

### Supporting Information

TEM characterization of aggregates, EDX spectra and additional STEM-EDX maps, schematic of integrating sphere showing T and R modes, absorbance of working electrodes before immersion in dye, photographs of nanoparticles and aggregates, calculated best fits of eq 6 to experimental *J*–*V* curves, and additional solar cell characterization details. This material is available free of charge via the Internet at <http://pubs.acs.org>.

## AUTHOR INFORMATION

### Corresponding Author

\*E-mail: [charles.schmittenmaer@yale.edu](mailto:charles.schmittenmaer@yale.edu) (C.A.S.); [hui.cao@yale.edu](mailto:hui.cao@yale.edu) (H.C.); [gary.brudvig@yale.edu](mailto:gary.brudvig@yale.edu) (G.W.B.).

### Notes

The authors declare no competing financial interest.

## ACKNOWLEDGMENTS

We acknowledge the Yale Climate and Energy Institute (YCEI) and an NSF Graduate Research Fellowship for support of this work. We thank Stephanie Tomasulo and Prof. Larry Lee for helpful discussions and technical assistance with IPCE measurements and Dr. Michael Rooks for technical assistance gathering STEM-EDX data. Facilities use was supported by the Yale Institute for Nanoscience and Quantum Engineering (YINQE) and NSF MRSEC DMR 1119826.

## REFERENCES

- (1) Willets, K. A.; Van Duyne, R. P. *Annu. Rev. Phys. Chem.* **2007**, *58*, 267–297.
- (2) Kreibig, U.; Vollmer, M. *Optical Properties of Metal Clusters*; Springer-Verlag: Berlin, 1995.
- (3) Ihara, M.; Tanaka, K.; Sakaki, K.; Honma, I.; Yamada, K. *J. Phys. Chem. B* **1997**, *101*, 5153–5157.
- (4) Kelly, K. L.; Coronado, E.; Zhao, L. L.; Schatz, G. C. *J. Phys. Chem. B* **2003**, *107*, 668–677.
- (5) Atwater, H. A.; Polman, A. *Nat. Mater.* **2010**, *9*, 205–213.
- (6) Ding, I. K.; Zhu, J.; Cai, W. S.; Moon, S. J.; Cai, N.; Wang, P.; Zakeeruddin, S. M.; Gratzel, M.; Brongersma, M. L.; Cui, Y.; McGehee, M. D. *Adv. Energy Mater.* **2011**, *1*, 52–57.
- (7) Kim, S. S.; Na, S. I.; Jo, J.; Kim, D. Y.; Nah, Y. C. *Appl. Phys. Lett.* **2008**, *93*, 073307.
- (8) Warren, S. C.; Thimsen, E. *Energy Environ. Sci.* **2012**, *5*, 5133–5146.
- (9) Qi, J. F.; Dang, X. N.; Hammond, P. T.; Belcher, A. M. *ACS Nano* **2011**, *5*, 7108–7116.
- (10) Peh, C. K. N.; Le, K.; Ho, G. W. *Mater. Lett.* **2010**, *64*, 1372–1375.
- (11) Standridge, S. D.; Schatz, G. C.; Hupp, J. T. *J. Am. Chem. Soc.* **2009**, *131*, 8407–8409.
- (12) Brown, M. D.; Suteewong, T.; Kumar, R. S. S.; D’Innocenzo, V.; Petrozza, A.; Lee, M. M.; Wiesner, U.; Snaith, H. J. *Nano Lett.* **2011**, *11*, 438–445.
- (13) Choi, H.; Chen, W. T.; Kamat, P. V. *ACS Nano* **2012**, *6*, 4418–4427.
- (14) Hou, W. B.; Pavaskar, P.; Liu, Z. W.; Theiss, J.; Aykol, M.; Cronin, S. B. *Energy Environ. Sci.* **2011**, *4*, 4650–4655.
- (15) Nahm, C.; Choi, H.; Kim, J.; Jung, D. R.; Kim, C.; Moon, J.; Lee, B.; Park, B. *Appl. Phys. Lett.* **2011**, *99*, 253107.
- (16) Du, J.; Qi, J.; Wang, D.; Tang, Z. Y. *Energy Environ. Sci.* **2012**, *5*, 6914–6918.
- (17) Ching, S.; Li, Q.; Xiao, X.; Wong, K. Y.; Chen, T. *Energy Environ. Sci.* **2012**, *5*, 9444–9448.
- (18) Jain, P. K.; El-Sayed, M. A. *Chem. Phys. Lett.* **2010**, *487*, 153–164.
- (19) Esteban, R.; Taylor, R. W.; Baumberg, J. J.; Aizpurua, J. *Langmuir* **2012**, *28*, 8881–8890.
- (20) Zook, J. M.; Rastogi, V.; MacCuspie, R. I.; Keene, A. M.; Fagan, J. *ACS Nano* **2011**, *5*, 8070–8079.
- (21) Shalae, V. M.; Botet, R.; Tsai, D. P.; Kovacs, J.; Moskovits, M. *Physica A* **1994**, *207*, 197–207.
- (22) Liz-Marzan, L. M.; Giersig, M.; Mulvaney, P. *Langmuir* **1996**, *12*, 4329–4335.
- (23) Underwood, S.; Mulvaney, P. *Langmuir* **1994**, *10*, 3427–3430.
- (24) Chen, H. J.; Kou, X. S.; Yang, Z.; Ni, W. H.; Wang, J. F. *Langmuir* **2008**, *24*, 5233–5237.
- (25) Jeong, N. C.; Prasittichai, C.; Hupp, J. T. *Langmuir* **2011**, *27*, 14609–14614.
- (26) Chen, H.; Blaber, M. G.; Standridge, S. D.; DeMarco, E. J.; Hupp, J. T.; Ratner, M. A.; Schatz, G. C. *J. Phys. Chem. C* **2012**, *116*, 10215–10221.
- (27) Davis, A.; Tran, T.; Young, D. R. *Hydrometallurgy* **1993**, *32*, 143–159.
- (28) Standridge, S. D.; Schatz, G. C.; Hupp, J. T. *Langmuir* **2009**, *25*, 2596–2600.
- (29) Lal, S.; Grady, N. K.; Goodrich, G. P.; Halas, N. J. *Nano Lett.* **2006**, *6*, 2338–2343.
- (30) Funston, A. M.; Novo, C.; Davis, T. J.; Mulvaney, P. *Nano Lett.* **2009**, *9*, 1651–1658.
- (31) Rand, B. P.; Peumans, P.; Forrest, S. R. *J. Appl. Phys.* **2004**, *96*, 7519–7526.
- (32) Markel, V. A.; George, T. F. *Optics of Nanostructured Materials*; Wiley: New York, 2001.
- (33) Sarychev, A. K.; Shalae, V. M. *Phys. Rep.* **2000**, *335*, 275–371.
- (34) Seal, K.; Genov, D. A.; Sarychev, A. K.; Noh, H.; Shalae, V. M.; Ying, Z. C.; Zhang, X.; Cao, H. *Phys. Rev. Lett.* **2006**, *97*, 206103.
- (35) Seal, K.; Sarychev, A. K.; Noh, H.; Genov, D. A.; Yamilov, A.; Shalae, V. M.; Ying, Z. C.; Cao, H. *Phys. Rev. Lett.* **2005**, *94*, 226101.

- (36) Schuller, J. A.; Barnard, E. S.; Cai, W. S.; Jun, Y. C.; White, J. S.; Brongersma, M. L. *Nat. Mater.* **2010**, *9*, 193–204.
- (37) Enustun, B. V.; Turkevich, J. *J. Am. Chem. Soc.* **1963**, *85*, 3317–3328.
- (38) Lee, J. W.; Kong, S.; Kim, W. S.; Kim, J. *Mater. Chem. Phys.* **2007**, *106*, 39–44.
- (39) Moore, G. F.; Konezny, S. J.; Song, H. E.; Milot, R. L.; Blakemore, J. D.; Lee, M. L.; Batista, V. S.; Schmittenmaer, C. A.; Crabtree, R. H.; Brudvig, G. W. *J. Phys. Chem. C* **2012**, *116*, 4892–4902.
- (40) Pena, O.; Pal, U. *Comput. Phys. Commun.* **2009**, *180*, 2348–2354.
- (41) Johnson, P. B.; Christy, R. W. *Phys. Rev. B* **1972**, *6*, 4370–4379.
- (42) Kraus, W. A.; Schatz, G. C. *J. Chem. Phys.* **1983**, *79*, 6130–6139.
- (43) Coronado, E. A.; Schatz, G. C. *J. Chem. Phys.* **2003**, *119*, 3926–3934.
- (44) Values of Drude parameters are taken from Reference 23:  $\omega_p = 1.44 \times 10^{16} \text{ s}^{-1}$ ,  $\gamma_0 = 1.075 \times 10^{14} \text{ s}^{-1}$ ,  $v_F = 1.4 \times 10^6 \text{ m/s}$ , and  $l_\infty = 13.0 \text{ nm}$ .
- (45) Soukoulis, C. M.; Datta, S.; Economou, E. N. *Phys. Rev. B* **1994**, *49*, 3800–3810.
- (46) Ito, S.; Chen, P.; Comte, P.; Nazeeruddin, M. K.; Liska, P.; Pechy, P.; Gratzel, M. *Prog. Photovoltaics* **2007**, *15*, 603–612.
- (47) Elguibaly, F.; Colbow, K.; Funt, B. L. *J. Appl. Phys.* **1981**, *52*, 3480–3483.
- (48) Shalaev, V. M. *Nonlinear Optics of Random Media: Fractal Composites and Metal-Dielectric Films*; Springer: Berlin, 2000.



## Supporting Information

### Plasmonic Enhancement of Dye-Sensitized Solar Cells using Core-Shell-Shell Nanostructures

*Stafford W. Sheehan,<sup>1</sup> Heeso Noh,<sup>2</sup> Gary W. Brudvig,<sup>1</sup> Hui Cao,<sup>2</sup> and Charles A. Schmuttenmaer<sup>1</sup>*

<sup>1</sup>Yale University Department of Chemistry, 225 Prospect St., PO Box 208107, New Haven, CT 06520-8107 USA

<sup>2</sup>Yale University, Department of Applied Physics, New Haven, CT 06511 USA

#### EDX Spectra and TEM Analysis

Nanostructured aggregates contain a varied number of gold nanoparticles in each cluster due to the uncontrolled nature of their aggregation. The aggregation occurs in a nonlinear fashion forming random fractal-like structures.

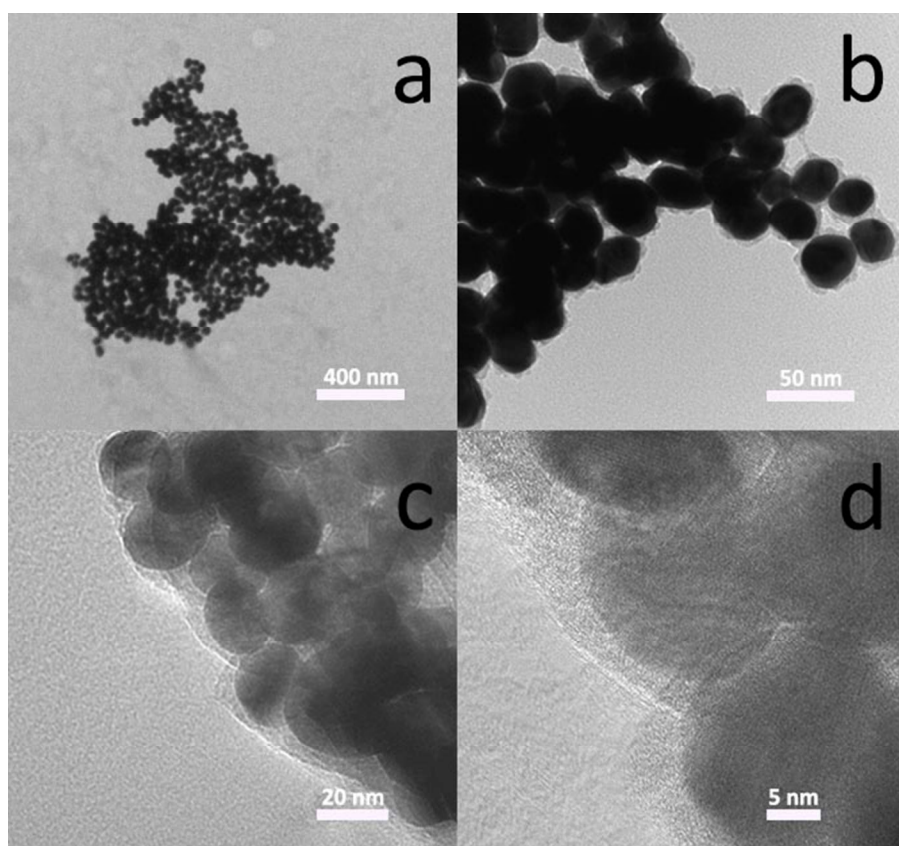


**Figure S1:** Low-resolution (a, b) and high-resolution (c, d) images of aggregate nanostructures at different magnifications. A thin layer of  $\text{TiO}_2$  can be seen on the outside of the nanoparticles in addition to the spaces between them where dye molecules can be anchored. Scale bars: (a): 400 nm, (b): 50 nm, (c): 20 nm, (d): 5 nm.

Additional EDX spectra were taken using STEM mode in addition to STEM-EDX mapping to confirm the structure of the Au@SiO<sub>2</sub>@TiO<sub>2</sub> nanoparticles. Data were collected from nanoparticles on a holey carbon support film on a Cu TEM grid (Ted Pella, Inc.) leading to C and Cu peaks in the spectra below.

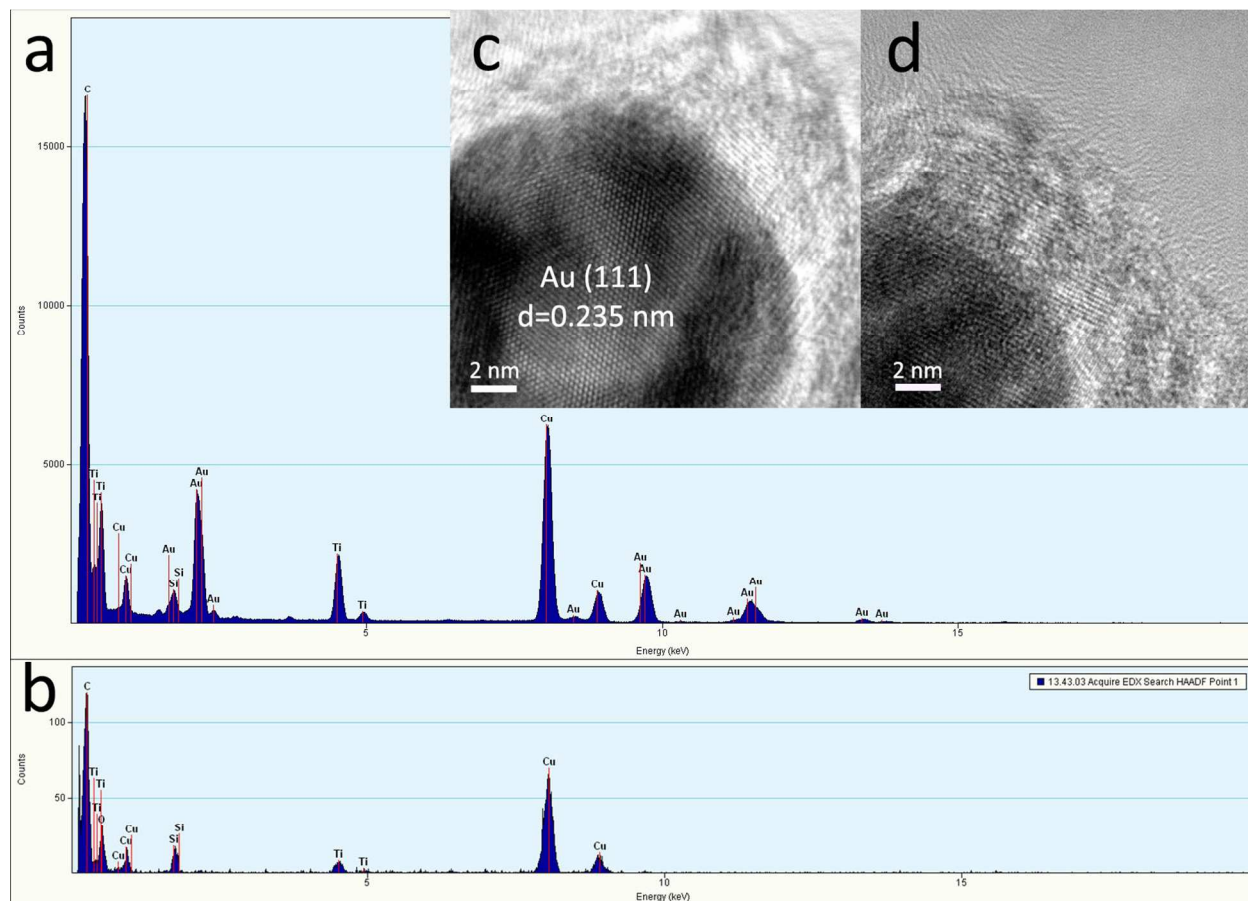


**Figure S2:** HRTEM and EDX spectra for Au@SiO<sub>2</sub>@TiO<sub>2</sub> (thin). Part (a) shows a spectrum when the electron beam is focused on a single nanoparticle. Au, Ti, and Si peaks are readily visible. Part (b) is a spectrum taken in STEM mode of the shells only, where only Si, Ti, and O can be seen. Parts (c) and (d) are HRTEM images of nanoparticles where their low degree of crystallinity in their shells is evident, particularly in contrast with the crystalline Au core (scale bars = 2 nm).

Au core, SiO<sub>2</sub> shell, and combined SiO<sub>2</sub>+TiO<sub>2</sub> shell sizes are shown below in Table S1.

Statistic	Mean	Standard Dev.
Au core size	18.09	2.45
SiO <sub>2</sub> shell size	1.61	0.78
Combined SiO <sub>2</sub> + thin TiO <sub>2</sub> shell size	4.09	1.19
Combined SiO <sub>2</sub> + thick TiO <sub>2</sub> shell size	8.56	2.31

**Table S1:** Statistics showing mean and standard deviation of counts of 100 nanoparticles inspected under TEM.

A breakdown of the components in the STEM-EDX map shown in Figure 2b can be seen below. The Au cores (green, part a) are encapsulated by SiO<sub>2</sub> (Si is represented in blue, part b), which is then further surrounded by a jagged layer of TiO<sub>2</sub> (Ti is represented in red, part c). A different STEM-EDX map of Au@SiO<sub>2</sub>@TiO<sub>2</sub> (thin) NPs is also shown, with both Si and Au detected in part (e) and Si, Au, and Ti detected in part (f) to more clearly illustrate the final TiO<sub>2</sub> shell around SiO<sub>2</sub>.

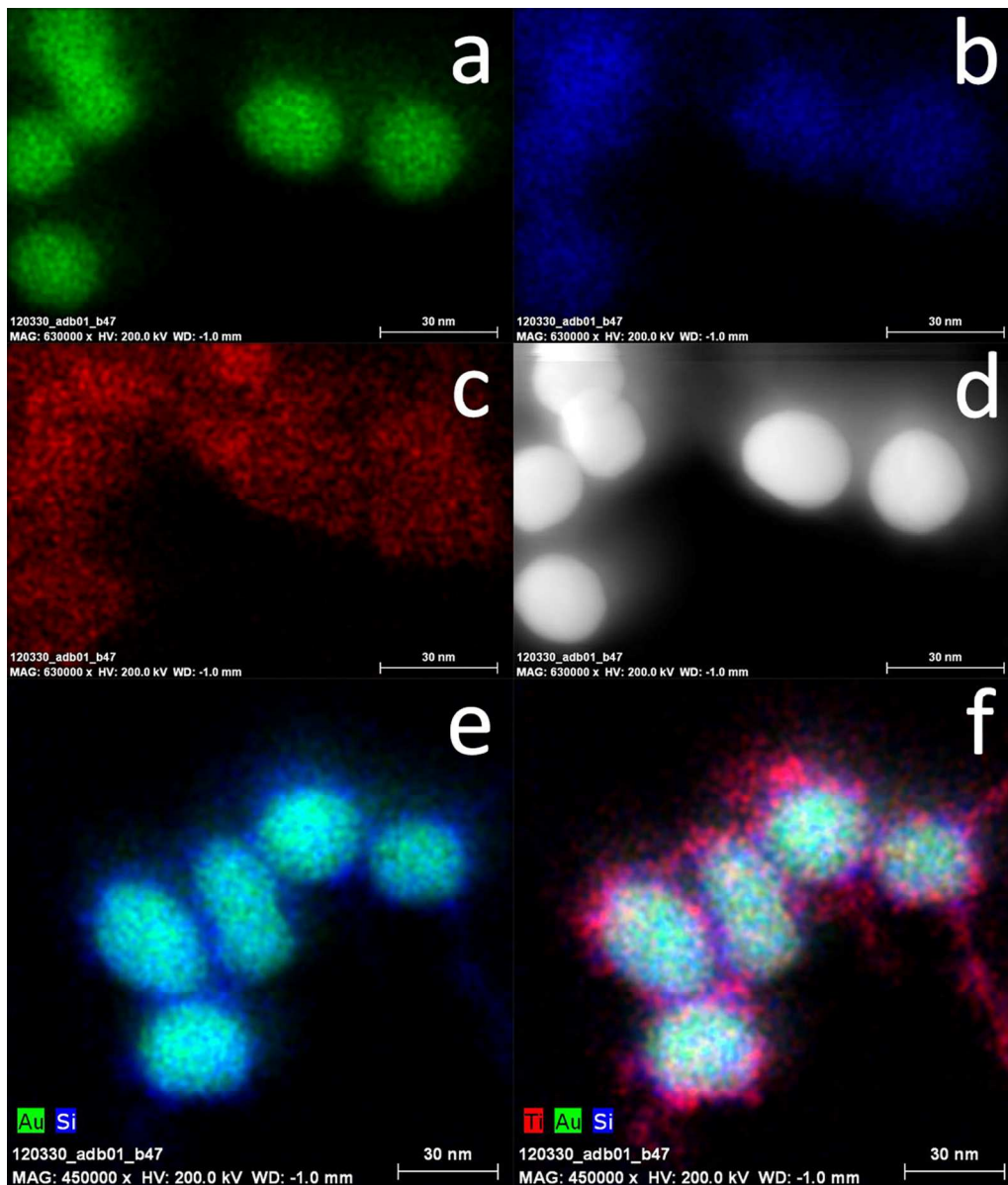


**Figure S3:** STEM-EDX maps of Au@SiO<sub>2</sub>@TiO<sub>2</sub> (thin) NPs. Au, Si, and Ti are represented in (a), (b), and (c), respectively, with the high-angle annular dark field image in (d). Different groups of nanoparticles are shown in (e) and (f) with the same color scheme for Au, Si, and Ti.



## Optical Measurements

In order to both determine qualitatively the concentration of NPs in the doctor-bladed working electrodes and show their changes in absorbance upon addition of dye, spectra shown below were taken of the films before immersion in N719 solution.

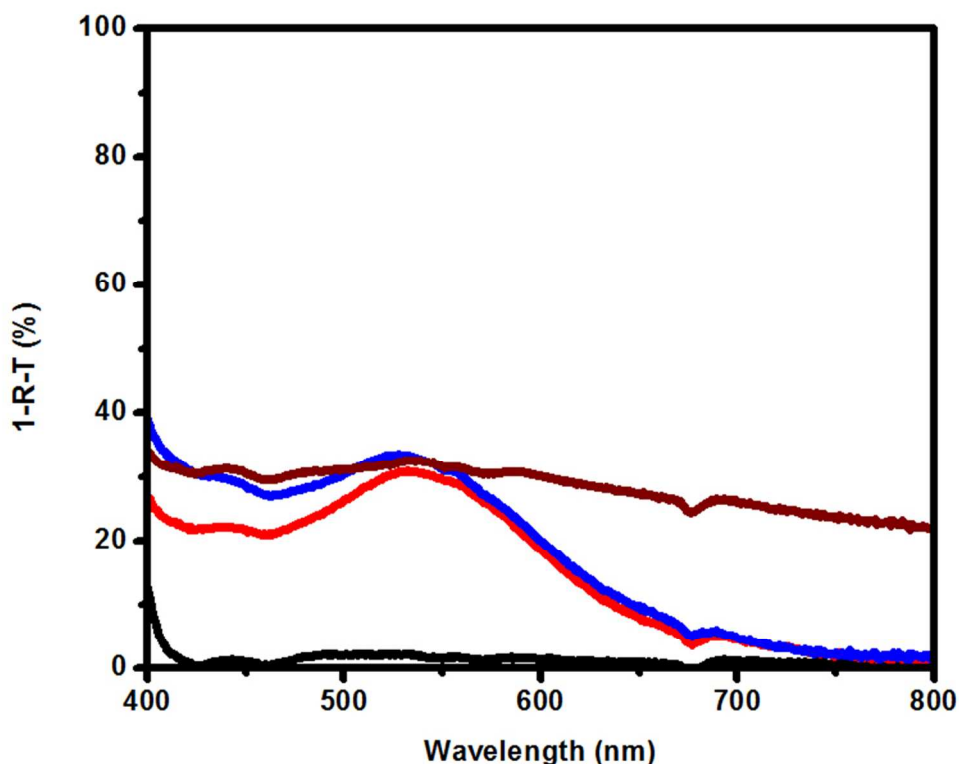


**Figure S4:** Absorbance spectra for films without dye showing relative concentrations of NPs in doctor-bladed films post-sintering at 400 °C. The same color scheme as used in Figures 5a and b is used: black, red, blue, and maroon represent P25 TiO<sub>2</sub> without NPs, with Au@SiO<sub>2</sub>, with Au@SiO<sub>2</sub>@TiO<sub>2</sub> (thin), and aggregate nanostructures, respectively.

Because of the highly scattering nature of these films, the reflectance,  $R$ , and transmittance,  $T$ , of the samples were measured individually as shown in Figure S5, and the absorbance,  $A$ , is calculated using the relation  $A + R + T = 1$ . The absorbance<sup>1</sup> is not to be confused with the absorbance, which is also typically denoted with the symbol  $A$ , and is defined as  $A = -\log(I/I_0)$  where  $I_0$  is the intensity incident on the sample and  $I$  is the transmitted intensity, and is only applicable when the reflectance is negligible.

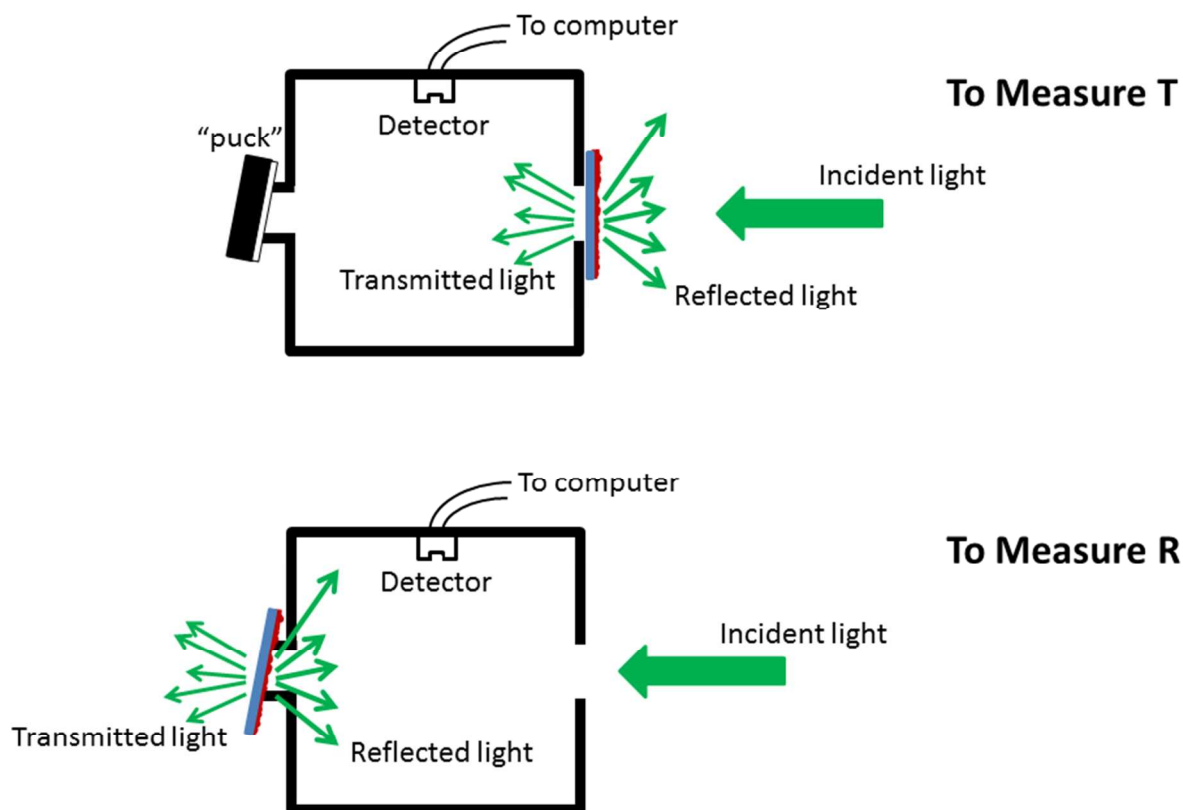


**Figure S5:** Schematic of integrating sphere showing T and R Modes.

The synthesis of the aggregates requires  $\sim 2$  hours of stirring in order to fully form. At the beginning of this period, the aggregates have a bluish color and a clear, broad peak centered at 680 nm due to coupled plasmonic modes between nanoparticles that continues to broaden until it encompasses the entire visible spectral region. This could be due to gradual increase in the size of the aggregates, thereby increasing the number of coupled modes and plasmonic ‘hot spots’ per nanostructure. Figure S6 shows the difference between absorption of the aggregates immediately after addition of  $\text{Ti}(\text{iPrO})_4$  and after they are stabilized. Figure S7 displays photos of the aggregates in a cuvette as well as  $\text{Au}@\text{SiO}_2$  NPs and  $\text{Au}@\text{SiO}_2@\text{TiO}_2$  (thin) NPs that clearly illustrate their dark black coloring and difference in color from the  $\text{Au}@\text{SiO}_2$  NP precursor.

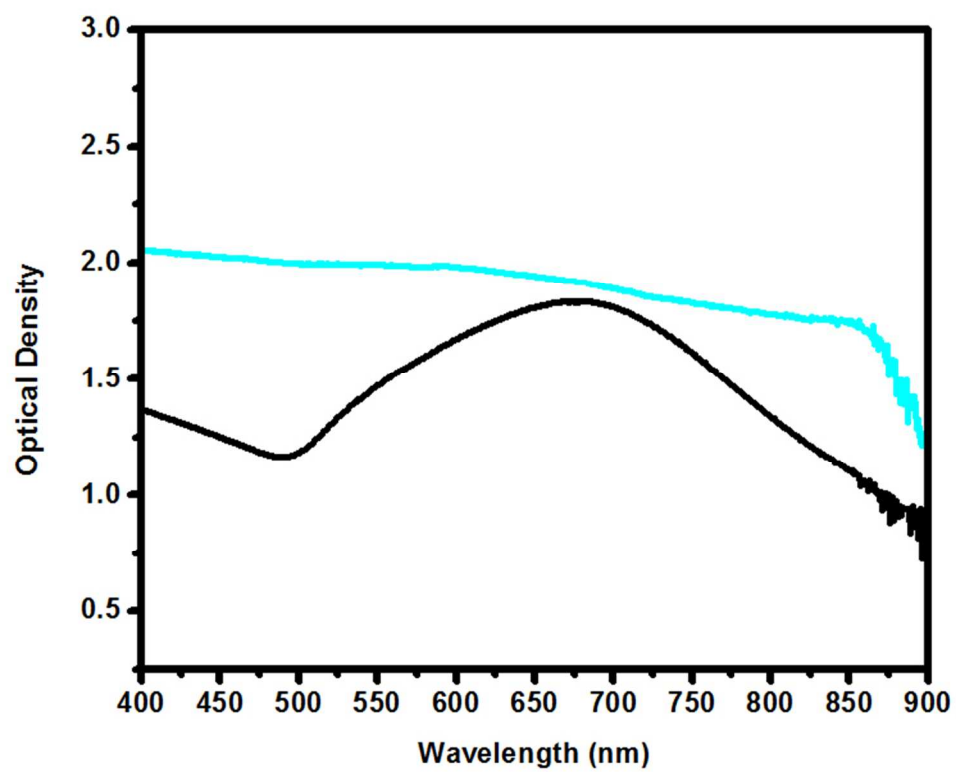


**Figure S6:** Absorbance spectra of aggregates immediately after adding  $\text{Ti}(\text{iPrO})_4$  (black) and after 2 hours (light blue).

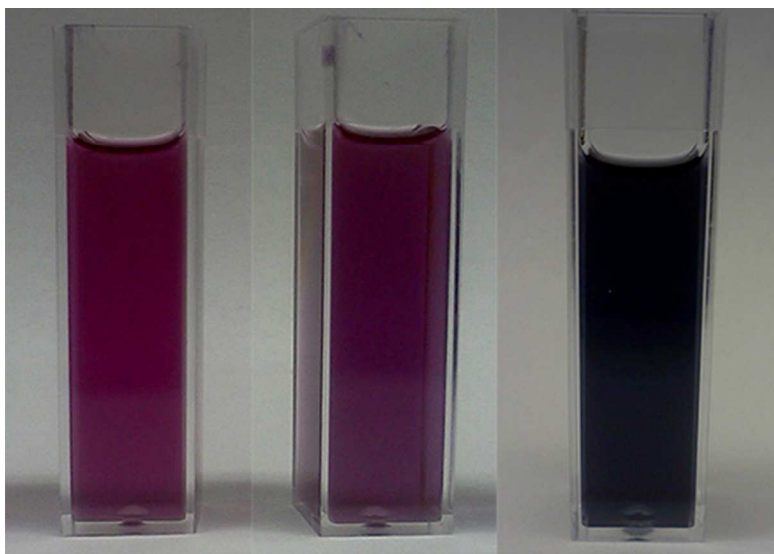


**Figure S7:** Photographs of Au@SiO<sub>2</sub> (left), Au@SiO<sub>2</sub>@TiO<sub>2</sub> (thin, middle), and aggregates (right) in ethanol.



## Solar Cell Characterization

All solar cell averages reported are the result of 9 solar cells made with their respective nanoparticles. Table 1 in the main text provides the averages, and Table S2 reports the standard deviations for each of the 4 batches of solar cells that incorporated different plasmonic nanoparticles, in addition to one control batch with no nanoparticles.

Nanoparticles in P25	$V_{oc}$ (V)	$J_{sc}$ (mA/cm <sup>2</sup> )	FF (%)	Avg Efficiency (%)
None	0.0368	0.716	4.95	0.339
Au@SiO <sub>2</sub>	0.0260	0.542	5.44	0.320
Au@SiO <sub>2</sub> @TiO <sub>2</sub> Thin	0.0472	1.780	9.34	0.326
Au@SiO <sub>2</sub> @TiO <sub>2</sub> Thick	0.0224	0.519	3.27	0.327
Aggregates	0.0500	1.311	3.57	0.699

**Table S2:** Standard deviations for solar cell parameters.

The averages, bests for each parameter, and standard deviations are plotted in Figure S8 for rapid comparison. Figure S9 and Table S3 show the results of fitting of the solar cell diode equation (eq. 6) to the experimental  $J$ - $V$  curves.

NP identities

1: None

2: Au@SiO<sub>2</sub>

3: Au@SiO<sub>2</sub>@TiO<sub>2</sub> Thin

4: Au@SiO<sub>2</sub>@TiO<sub>2</sub> Thick

5: Aggregates

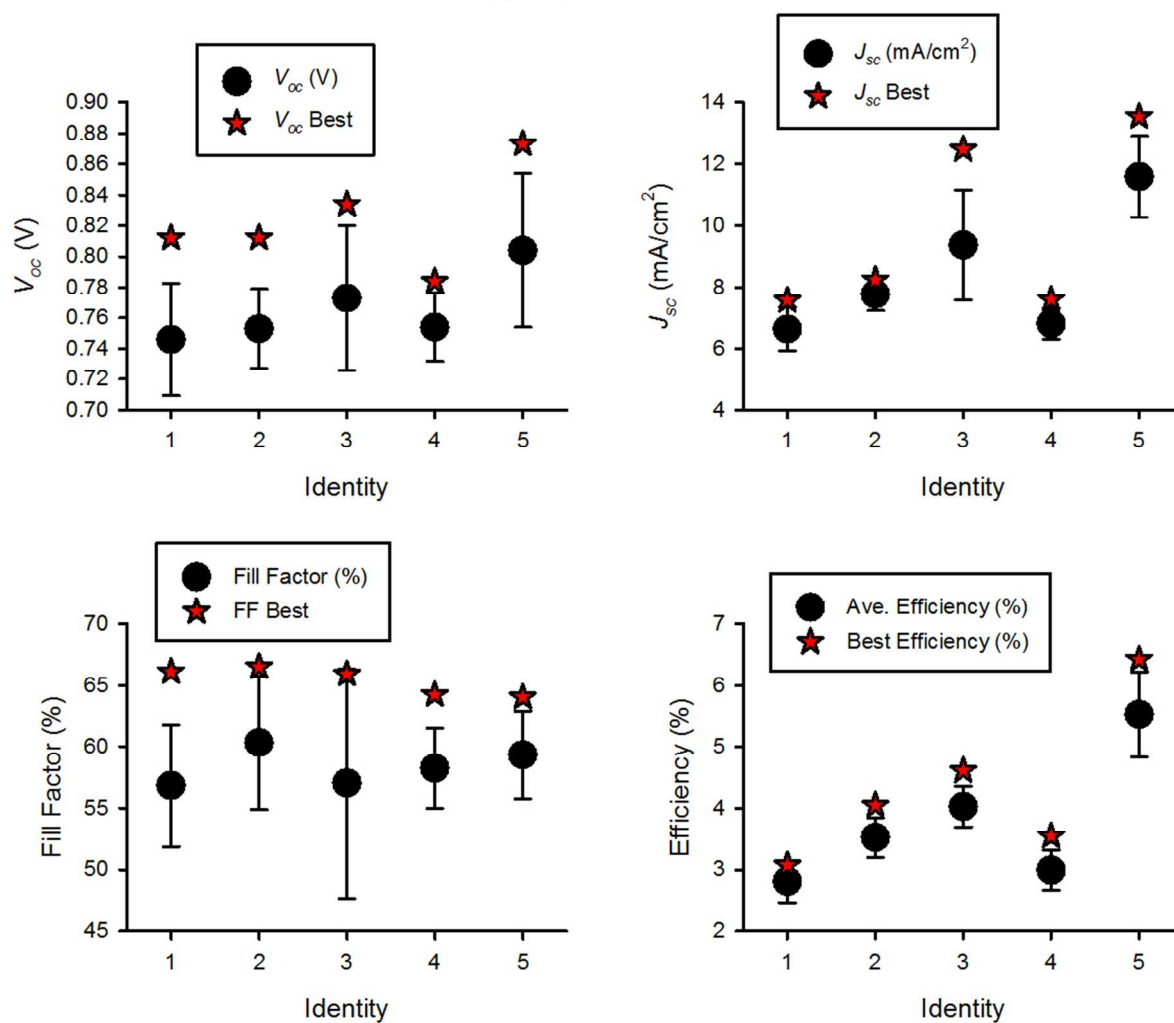
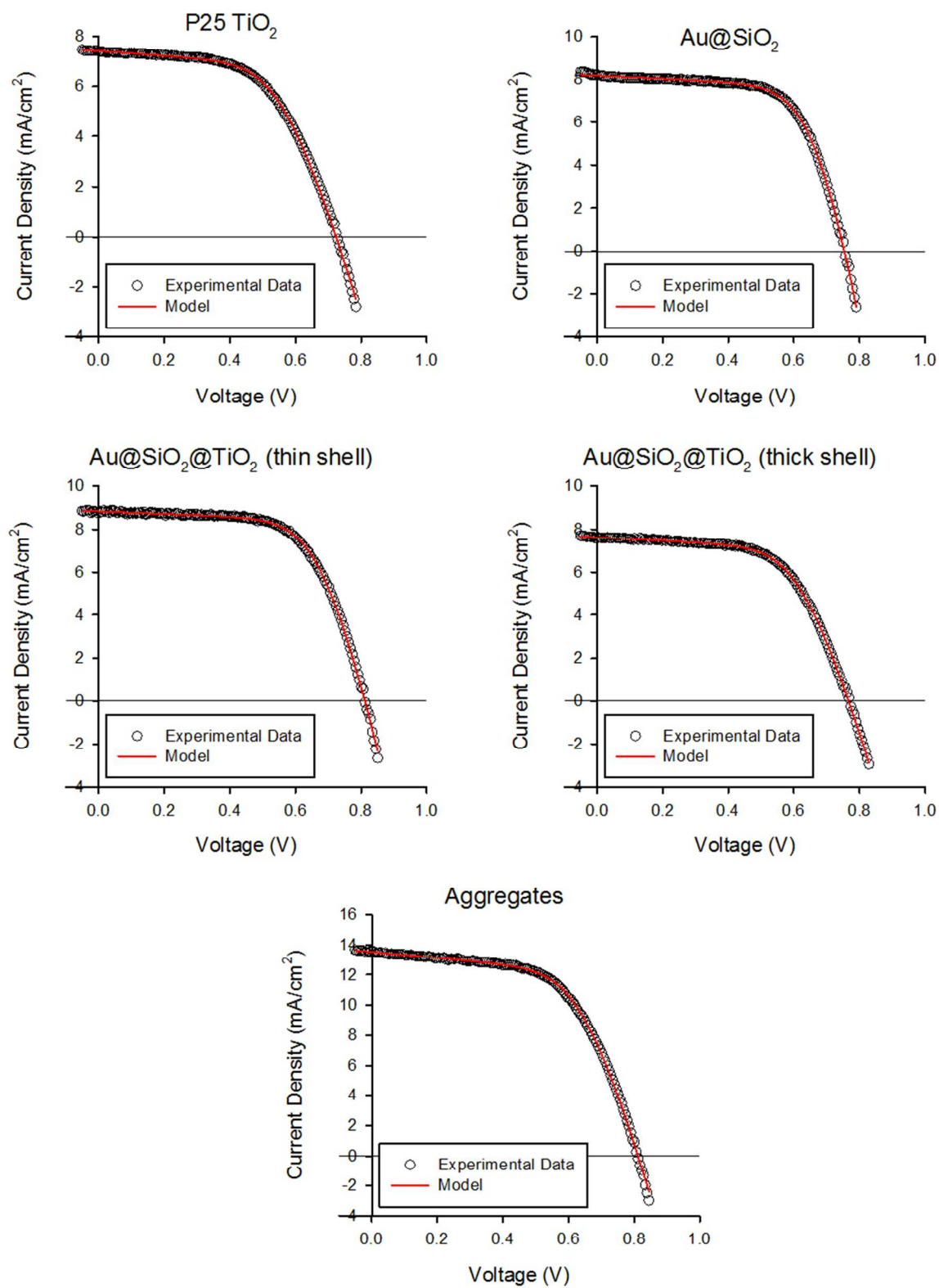


Figure S8: Plot of solar cell parameters.



**Figure S9:** Experimental vs. calculated  $J$ - $V$  curves for ‘Best’ solar cells.



Parameter	P25 TiO <sub>2</sub>	Au@SiO <sub>2</sub>	Au@SiO <sub>2</sub> @TiO <sub>2</sub> (thin)	Au@SiO <sub>2</sub> @TiO <sub>2</sub> (thick)	Aggregates
J <sub>0</sub> (mA/cm <sup>2</sup> )	7.85E-06	4.98E-06	1.83E-06	3.61E-06	2.64E-06
J <sub>L</sub> (mA/cm <sup>2</sup> )	7.5461	8.2174	8.8905	7.7258	13.817
R <sub>s</sub> (Ω)	17.9	8.26	11.4	15.3	10.2
R <sub>sh</sub> (Ω)	1046.4	1360.5	1700.6	1245.9	484.2
T (°C)	25	25	25	25	25
f (ideality)	2	2	2	2	2
Chi squared	1.915	1.592	3.003	0.669	6.601

**Table S3:** Fitting parameters for ‘Best’ solar cells.

Only the ‘Best’ curves were chosen because the ‘Average’ curves have unrealistic fill factors, since they do not average linearly in the same way J<sub>sc</sub> and V<sub>oc</sub> do.

## REFERENCES

- (1) IUPAC. IUPAC. Compendium of Chemical Terminology, 2nd ed. (the "Gold Book"). Compiled by A. D. McNaught and A. Wilkinson. Blackwell Scientific Publications, Oxford (1997). XML on-line corrected version: <http://goldbook.iupac.org> (2006-) created by M. Nic, J. Jirat, B. Kosata; updates compiled by A. Jenkins.